ARMA 13-729

Predicting the Paleo Evolution of Overpressured Geological Structures

Rance, J.M. and Profit, M.L.
Rockfield Software Limited, Swansea, Wales, UK
Dee, S.J.
BP, Sunbury, England, UK
Roberts, D.T.
Cardiff University, Cardiff, Wales, UK

This paper was prepared for presentation at the 47th US Rock Mechanics / Geomechanics Symposium held in San Francisco, CA, USA, 23-26 June 2013.

ABSTRACT: Forward modeling the formation of geological structures can provide additional insight into their evolution. The ability of these models to replicate the evolution without the requirement for seeding means that important information relating to the material state and development of, or absence, of overpressures can be extracted. Case studies are presented relating to forward modeling the evolution of the ACG anticline using the Finite/Discrete Element software package ELFEN. 2D sections are modeled with the software under a variety of conditions. Modeled pore pressure distribution with depth is compared to a reference with favorable results. Final geometries interpreted from seismic data also match model predictions.

1. INTRODUCTION

The ability to predict the physical formation of geological structures provides significant benefit in understanding the evolution of stress and pore pressure distribution within a field and, in particular, the material state of the reservoir units. Geometric or kinematic techniques are often used to analyse geological structures but they ignore the mechanical deformation response of the rock strata. In some cases this may lead to the mechanisms responsible for the presence of a particular structure not being fully understood, or missed completely, with obvious implications for activities such as hydrocarbon exploration.

The emerging numerical and physics based forward modeling technology in ELFEN [1] overcomes these shortcomings and its techniques can be applied to study a wide range of complicated geological systems; from the interaction of deepwater sedimentary systems and salt structures [2] to tectonic driven folding and faulting [3]. The technology within ELFEN adopts a finite strain Lagrangian finite element formulation to represent the kinematics of deformation and when complemented by efficient automated adaptive remeshing techniques is able to capture localizations [4]. Development of the software has been undertaken with consideration of the range of processes which commonly influence the evolution of geological structures e.g. deposition, erosion. An advanced critical state material model, which links shear strength and compaction to volume change, captures the mechanical response of sedimentary layers. This has the crucial advantage of permitting the technology to capture naturally forming geological structures without having to seed the model. The modeling strategy has been successfully employed recently for the investigation of basement controls on faulting and folding [3,5].

Recent advances to the earlier forward modeling approach [6] have included the full coupling of the hydro and mechanical (HM) fields. This coupling accounts for the pore pressure changes arising from

the geomechanical deformation which naturally occur during sedimentation and erosion processes and tectonic activity.

The HM forward modeling technology has been applied to simulate the formation of the ACG (Azeri, Chirag, Gunashli) anticline. In the ACG anticline, the layers that make up the hydrocarbon reservoir section are understood to be in an overpressured state prior to production as a consequence of recent rapid sedimentation and lateral shortening. A forward model has been produced of the ACG anticline that captures the combined geomechanical and porous-flow evolution. It has been employed to investigate the influence of various physical parameters such as lateral shortening, sedimentation rates, basal evolution timings and strata constitutive properties on the overpressured pore pressure distribution and the formation of structures above the crest.

2. GEOMECHANICAL MODELING

2.1. Introduction

The computational modeling employs ELFEN's nonlinear finite element system that comprises procedures for both implicit and quasi-static explicit simulation of finite strain applications and quasi-brittle localizations. The general procedures have been previously presented in a number of publications [4,6,7,8].

The computational approach is based on the Lagrangian method with automatic remeshing to alleviate element distortion and improve solution accuracy. The key features for the current application are:

1. Critical state constitutive model
2. Capability to capture localizations (e.g. faulting)
3. Coupling between mechanical behavior and porous flow

2.2. Constitutive Modeling

The geomaterial layering is represented by ELFEN's SR3 critical state constitutive model. The material model is a single surface, rate independent, non-associative elasto-plasticity model. It is formulated such that additional effects such as anisotropy, creep and damage can be added to the base model. A typical yield surface definition in *p-q* (effective mean stress versus deviatoric stress) space is shown in Fig. 1. The primary yield surface function ϕ is a smooth three-invariant surface that intersects the hydrostatic axis in both tension and compression and is defined as:

$$\phi(\boldsymbol{\sigma}, \varepsilon_v^p) = gq + (p - p_t)tan\beta \left(\frac{p - p_c}{p_t - p_c}\right)^{1/n} \quad (1)$$

where p is the effective mean stress, q is the deviatoric stress, p_t is the tensile intercept of the yield surface with the hydrostatic axis, p_c is the pre-consolidation pressure or compressive intercept of the yield surface with the hydrostatic axis, β and n are material constants which define the shape of the yield surface in the p-q plane and g is a function that controls the shape of the yield function in the deviatoric plane [6].

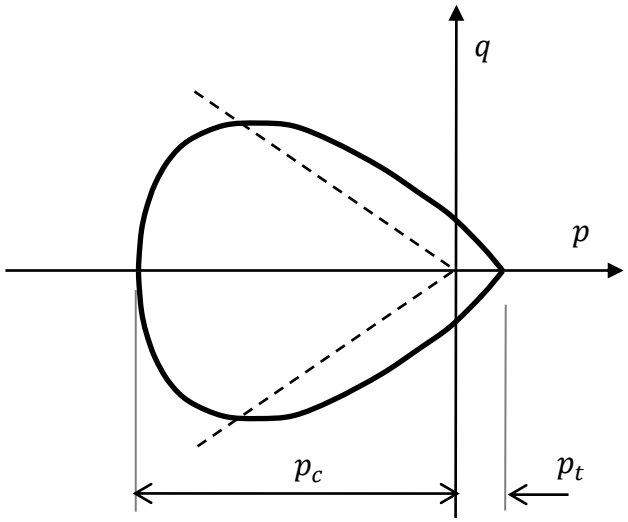

Fig. 1. SR3 Yield Surface

The evolution of the pre-consolidation pressure is governed by the specific volume υ or volumetric plastic strain ε_v^p:

$$p_c = p_{c0} exp\left[-\frac{\upsilon \varepsilon_v^p}{\lambda - \kappa}\right] \quad (2)$$

where p_{c0} is the initial pre-consolidation pressure, λ and κ are the slopes of the normal compression line (ncl) and the unloading-reloading line (url) in υ vs. $\ln p$ space, respectively. A similar expression exists for the evolution of p_t [6].

2.3. Capturing Localizations

Localization of deformation towards discrete planes arise naturally in finite element simulations from the continuum response of the geomaterial, so that the creation of shear banding and the initial direction of the shear bands can be simulated in a relatively straightforward fashion; extension of

work in [9]. Accurate representation of localizations and evaluation of the energy dissipation in the post-localization configuration is, however, more difficult using standard continuum approaches, due to a number of well-known issues:

1. The direction of propagation may be severely biased by the direction of the grid lines; e.g. localizations aligned with the element edges or element diagonals.
2. Energy dissipation by both mode-I and mode-II deformation on the localization bands is very sensitive to the fineness of the localizations; i.e. the solutions are dependent on the *element length* rather than a physical *material length scale*.
3. Large shear movement on the localizations results in excessive mesh distortion which can cause an early termination of the solution unless remeshing is invoked.

There are many different modeling strategies which can be employed to overcome the first and second deficiencies and these can be classified based on the relative size of the finite element (*h*) and the width of the localization band (*b*) [10]:

1. Sub-*h* – the localization bandwidth is smaller than the element size; e.g. finite/discrete element methods
2. Iso-*h* – the element size is chosen to equal the localization bandwidth; e.g. adaptive remesh strategies
3. Super-*h* – the localization bandwidth is larger than the element size, where the width of the localization band is determined by the fine discretization; e.g. non-local models, Cosserat continuum and gradient plasticity methods.

Sub-*h* formulations are essential for the majority of practical rock mechanics applications as the fracture or fault is finite, but generally very thin relative to the structural dimension; i.e. the localization will generally be confined to a single element.

In the fracture energy approach, which is adopted in this study, the global energy dissipation is regularized by including fracture energy as a material constant in the equations governing the state variable evolution.

2.4. Coupled Geomechanics and Flow

The computational approach adopts a Lagrangian (material) reference for the solid phase and a Eulerian (spatial) reference frame for the porous flow phase. The fluid velocities $\boldsymbol{v}_f$ and accelerations $\boldsymbol{a}_f$ are therefore referred to the solid phase as:

$$\boldsymbol{v}_f = \boldsymbol{v}_{fs} + \boldsymbol{v}_s \tag{3}$$

$$\boldsymbol{a}_f = \boldsymbol{a}_{fs} + \boldsymbol{a}_s \tag{4}$$

where the subscript s denotes the solid phase and v_{fs} and a_{fs} are the velocity and acceleration of the fluid phase relative to the solid phase respectively. By neglecting $\boldsymbol{a}_{fs}$ (i.e. assuming $\boldsymbol{a}_f = \boldsymbol{a}_s$) and noting that the moving Lagrangian solid frame allows the convective term to be omitted, it can be shown that with a single phase liquid the coupled system is represented by a dynamic equilibrium equation for the porous solid phase and a transient equilibrium equation for the fluid phase, i.e. [11]:

$$\begin{aligned} div\big(\boldsymbol{\sigma}' - \alpha(\phi)\mathbf{m}p_f\big) \\ + \big[(1-\phi)\rho_s + \phi\rho_f\big](\mathbf{g} - \boldsymbol{a}_s) \\ = 0 \end{aligned} \tag{5}$$

$$\begin{aligned} div\left(\frac{k(\phi)}{\mu_f(T)}\Big(\nabla p_f - \rho_f(\mathbf{g} - \boldsymbol{a}_s)\Big)\right) \\ = \left(\frac{\phi}{K_f} + \frac{\alpha(\phi) - \phi}{K_s}\right)\frac{\partial p_f}{\partial t} \\ + \alpha\frac{\partial \varepsilon_v}{\partial t} \end{aligned} \tag{6}$$

where ρ_s and ρ_f are the solid and fluid densities respectively, $\mathbf{g}$ is the gravitational vector, $\boldsymbol{\sigma}'$ is the effective stress, ϕ is the material porosity, $\alpha(\phi)$ is the porosity dependent Biot constant, $\mathbf{m} = \{1\,1\,1\,0\,0\,0\}^{\mathrm{T}}$, $k(\phi)$ is the porosity dependent intrinsic permeability, T is the pore fluid temperature, $\mu_f(T)$ is the temperature dependent pore fluid viscosity, K_f is the bulk modulus of the liquid, K_s is the bulk modulus of the solid particles, and ε_v is the volumetric strain.

For sedimentary rocks permeability is generally transversely isotropic and aligned with the bedding. The ratio between the bedding parallel permeability, k_{bed}, and bedding normal permeability, k_{norm}, is in the range $2 < k_{bed}/k_{norm} < 10$ for clastic rock and $1 < k_{bed}/k_{norm} < 3$ for carbonates [12].

Eqns (5) and (6) are coupled in a staggered sense. The mechanical governing equation is solved explicitly whilst its porous flow equivalent is solved implicitly. This implies that the time step which dictates the forward march of the mechanical

solution is only conditionally stable, whilst the seepage solution time step is unconditionally stable. The volumetric strain rate term in Eqn. (6) is very important in the generation of overpressure. Changes in volumetric strain, as a consequence of material dilation or compaction, directly relate to changes in pore space and hence pore pressure if pore fluid cannot drain fast enough. The volumetric strain rate term is responsible for a strong coupling between the geomechanical and pore fluid fields.

$$\boldsymbol{\sigma}' = \boldsymbol{\sigma} - \alpha(\phi)\boldsymbol{m}p_f \quad (7)$$

$$\Delta\varepsilon_v = f\left(\boldsymbol{\sigma}', p_f\right) \quad (8)$$

$$p_f = f\left(\alpha(\phi)\frac{\partial\varepsilon_v}{\partial t}\right) \quad (9)$$

This strong coupling manifests itself through the influence of pore pressure on the effective stress (in the geomechanical field), whilst the volumetric strain is a function of the effective stress (in the geomechanical field), and the pore pressure is dependent upon the volumetric strain (in the flow field). This is shown in Eqn. (7) - Eqn. (9).

3. APPLICATION OF FORWARD MODELING TECHNOLOGY

In the ACG anticline, the layers that constitute the hydrocarbon reservoir section are understood to be in an overpressured state prior to production. Overpressure is thought to have developed as a result of both recent rapid sedimentation and substantial tectonic shortening. The regional tectonic compression arises from the influence of a subduction zone 1000km to the NE of the anticline.
As a tool to understand the development of the raised pressures and their significance for the evolution of the anticline formation a forward model has been produced that captures the combined geomechanical and porous-flow evolution. The model has been developed to represent the formation of the ACG anticline considering a 2D plane section (23km long) parallel to the anticline over a period of 6Ma. Investigations using the model have been carried out to study the influence of various physical parameters such as lateral shortening (Fig. 2), sedimentation rates, basal evolution timings and strata constitutive properties. Many cases have been considered, however, only six cases are reported here. A forward model comprises an initial geometry representative of the lithology at a selected paleo-time and a sequence of sedimented layers added to the geometry as the simulation advances to the present day (Fig. 3).

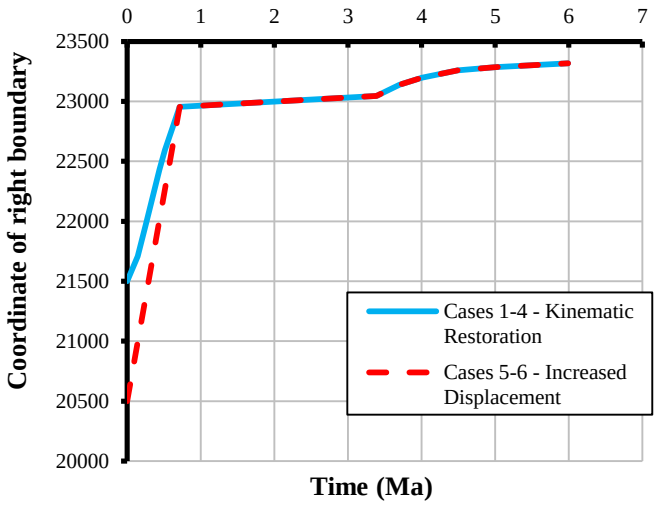

Fig. 2. Tectonic shortening of right hand boundary.

Gravitational forces are applied to each layer accounting for the compaction of the material as the overburden increases in depth. The side boundaries of the model may be compressed or extended by prescribed movement, representative of tectonic shortening and extension. The profile of the model's basement may be changed over the duration of the simulation. This is accomplished by defining the geometric profile of the basement at selected times and interpolating the displacement of the basement between defined profiles.

3.1. Basal Movements and Tectonic Definition

The formation of structures within the ACG model is driven through prescribed evolving basal profiles and tectonic shortening of the model side boundaries (Fig. 3). The basal surfaces have been constructed from kinematically restored horizons, with enhancements based on the findings of the forward modeling predictions. Initially, the tectonic shortening was consistent with the restored basal movement. In some cases (Case 2, 4 & 6) a frictionless contact surface was introduced between the basal surface and the model base, thus allowing non-linear basal strains to develop. Restoration techniques do not consider the possible compaction of the sediments due to the tectonic shortening

[13,14]. Therefore sensitivity studies were undertaken where increased lateral shortening of the model was considered.

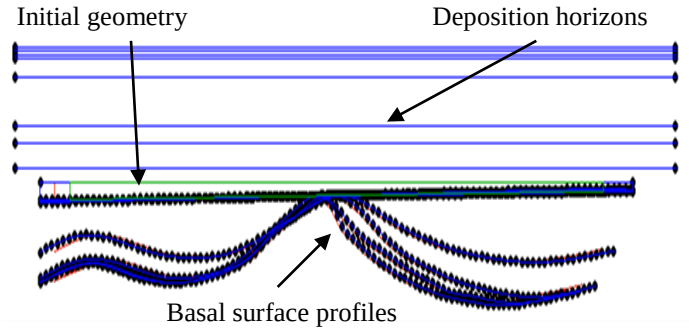

Fig. 3. Kinematically restored basal surfaces, initial geometry and deposition horizons.

Initially the tectonic shortening was thought to have occurred at a low rate until 0.72Ma ago which was followed by a rapid increase (see Fig. 2). In tandem with the initial low shortening rate the basal surface evolves into a gentle anticline fold, Fig. 3, from about 3.4Ma until 0.72Ma. As the shortening rate increases from 0.72Ma the limbs of the anticline steepen with a noticeable kink on the right limb.

3.2. Modeled Stratigraphy

Present day horizon heights and porosities are derived from a well located 1km from the crest of the anticline (Table 1). The stratigraphy of the model was defined by 11 sedimentary sequences. This comprised of 5 reservoir layers containing mainly sandstones and shales, and 6 overburden layers consisting of a selection of mudstones, shales, siltstones and gypsum evaporates. In all case studies the stratigraphy and sedimentation rates were as detailed in Table 1. Forward modeling requires uncompacted horizon heights to be specified in the model since the analysis algorithms capture the deposition and subsequent volume loss due to the compaction process. The uncompacted heights are calibrated from measured current day unit heights using an iterative process. This iterative process simulates the sedimentation sequence of a representative stratigraphic column and the modeled final heights are compared against the current day horizons. The uncompacted heights are then adjusted and the process repeated until a good match between model and physical data is achieved. Overpressure in fold structures is caused by a number of physical processes including chemical reactions, generation of hydrocarbon, lateral transfer along more permeable horizons, uplift tectonic stress and hydrodynamic effects. The most significant cause is, however, compaction disequilibrium where the sediment load builds more quickly than the fluid can escape [12]. On the ACG structure, very rapid sedimentation rates, and tectonic shortening are inferred.

3.3. Material Data

All material responses of the sedimentary layers are represented by the Soft-Rock 3 (SR3) model, as described in section 2. Property data for each layer reservoir unit (10 in total) was characterized using triaxial data as a foundation. In the case of the overburden, all 6 layers were assigned a unified property set, typical of shale/sandstone/mudstone response (Table 1).

Horizon	Lithology	Age (Ma)	True stratigraphic thickness (m)
Present	Shale/Mudstone/Sandstone	0.00	250
Kink Out	Shale/Mudstone/Sandstone	0.24	220
Late Shortening	Shale/Mudstone/Sandstone	0.48	335
Apsheron	Shale/Mudstone/Sandstone	0.72	330
Surakhany	Shale/Mudstone/Sandstone	3.40	605
Subunchi	Shale/Mudstone/Sandstone	3.70	285
Reservoir Series 1A	Sandstone	4.00	144
Reservoir Series 1B	Sandstone	4.10	250
Reservoir Series 1B	Shale	4.20	70
Reservoir Series 1C	Sandstone	4.30	40
Reservoir Series 1D	Sandstone	4.40	130
Reservoir Series 1D	Shale	4.50	120
Reservoir Series 1E	Sandstone	4.75	50
Reservoir Series 1E	Shale	5.00	55
Reservoir Series 2A	Sandstone	5.25	50
Reservoir Series 2B	Sandstone	5.50	60

Table 1. Horizon lithology, age and true stratigraphic thickness for a reference well.

For the coupled geomechanical-seepage studies the permeability of each stratigraphic unit was defined as transverse isotropic. Data supplied provided the permeability data for the reservoir layers and the porosity-permeability trend for the reservoir series 2a layer in the in-plane bedding direction. The porosity-permeability trend is typical for sandstone and therefore the same trend was used to calibrate the other layers. In the direction normal to the bedding plane the permeability was defined as a ratio (10 multiple) of the in-plane value as is typical of clastic rocks [12].

4. RESULTS OF CASE STUDIES

Numerous sensitivity studies have been undertaken enabling the influence of several parameters to be investigated on the horizon profiles, development (or absence) of overpressures and formation of structures above the anticline ridge. Presentation of the full suite of results is beyond the scope of this paper. Consequently, only a selection of the cases studied are presented in order to demonstrate the benefits of forward modeling in assessing various geological hypotheses proposed for the formation of the anticline. Specifically, evolution of the anticline based on kinematically restored tectonic movements for both drained (cases 1,3,5) and fully-coupled (cases 2,4,6) analyses are presented. In addition, the effect of non-uniform lateral strain at the basal surface (cases 3,4,5,6) and additional tectonic lateral shortening (cases 5,6) of the strata are presented. The pore pressure, effective plastic strain, effective vertical stress and effective horizontal stress contour keys which are used in sections 4.1 to 4.6 are shown in Fig. 4(a).

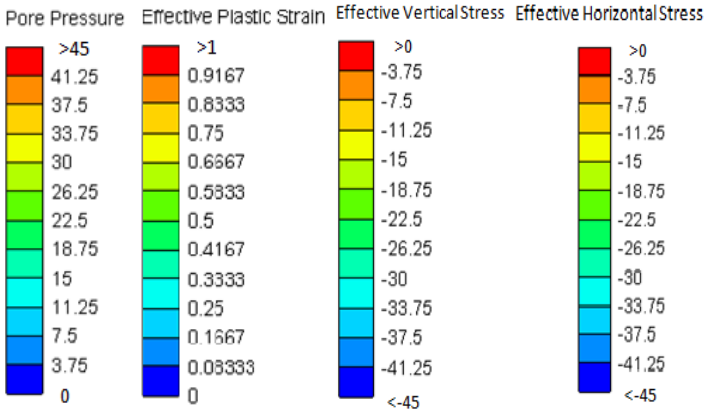

Fig. 4. (a) Contours of effective stresses (MPa), pore pressure (MPa)and effective plastic strains for use in sections 4.1 to 4.6.

Fig 4(b) is shown below and displays the locations of the overburden and reservoir layers.

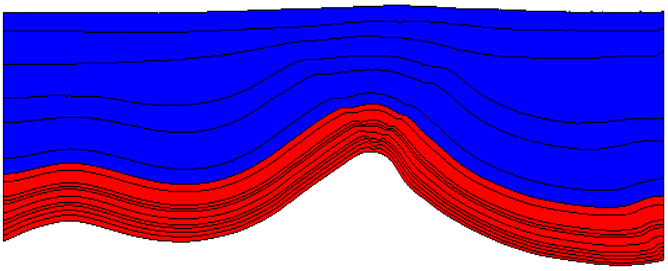

Fig. 4. (b) Image of current day ACG geometry (model output) showing 6 reservoir layers (red) and 10 overburden layers (blue).

4.1. Case 1 - Kinematically Restored Basal Surface - Geomechanical Drained

Case 1 adopts the original restoration surfaces and a mechanical only analysis which assumes the response of all layers is drained i.e. sedimentation rates and lateral shortening are assumed to be sufficiently slow to allow dissipation of fluids from the pore space. Results are presented below at times of 3.4Ma, 0.72Ma and Present Day for both vertical and horizontal effective stress as well as plastic strain (which is an indicator of shear localization and compaction) - see Fig. 5 & Fig. 6. The vertical effective stress distribution at time 3.4Ma is approximately lithostatic. As the anticline evolves (0.72Ma) the horizontal effective stress reduces significantly above the crest whilst the vertical effective stress remains lithostatic with a compressive zone developing either side of the crest near the basal surface.

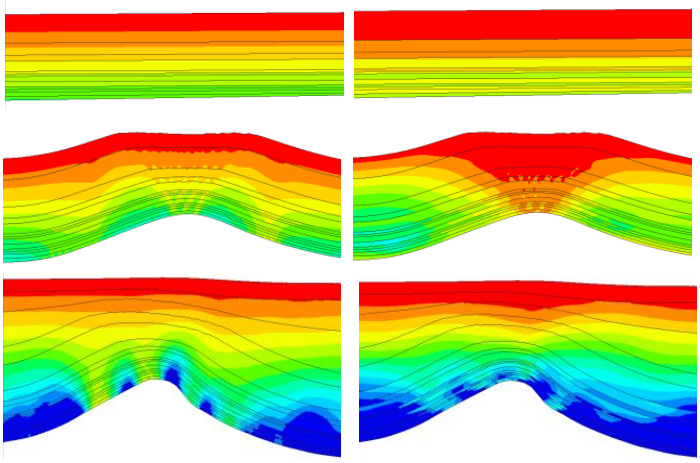

Fig. 5. Vertical (left) & horizontal (right) effective stress distribution at times 3.4Ma (upper), 0.72Ma (middle) and present day (lower) for Case 1.

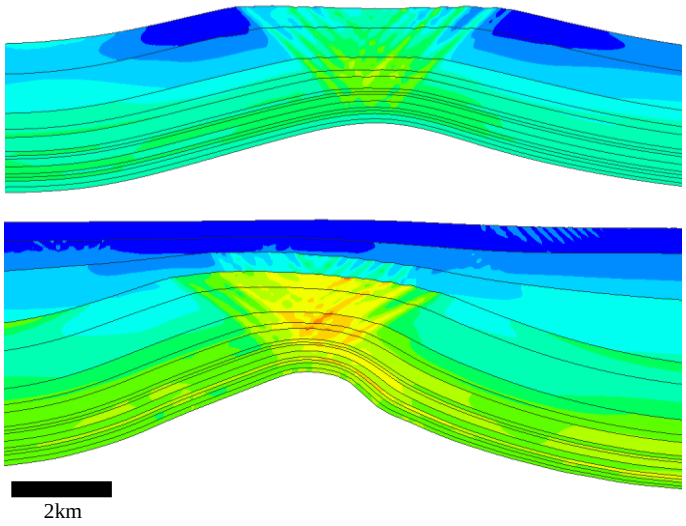

Fig. 6. Effective plastic strain at times 0.72Ma (upper) and present day (lower) for Case 1.

Further down the limbs of the anticline the vertical effective stress reduces below the lithostatic value due to stress re-orientation with the maximum principle stress normal to the basal surface. After further deposition, folding, and lateral shortening, the horizontal effective stress increases above the crest and tends towards a linearly increasing distribution.

As a consequence of the reduction in horizontal effective stress and rise in the deviatoric stress, at time 0.72Ma a graben structure is formed as indicated by the concentrated bands of plastic strain depicted in Fig. 6. This structure does not significantly develop to the current day, indicated by the modest offset on the fault, even though there is further folding at the crest.

4.2. Case 2 - Kinematically Restored Basal Surface - Geomechanical-Seepage Coupled

The stress distributions are similar (in pattern but differ in magnitude) to the previous case, as is the shear localization above the crest. Accounting for the seepage flow during the formation of the anticline leads to a reduction of both the vertical and horizontal effective stresses, Fig. 7, as overpressures are developed in the region of the crest (Fig. 8).

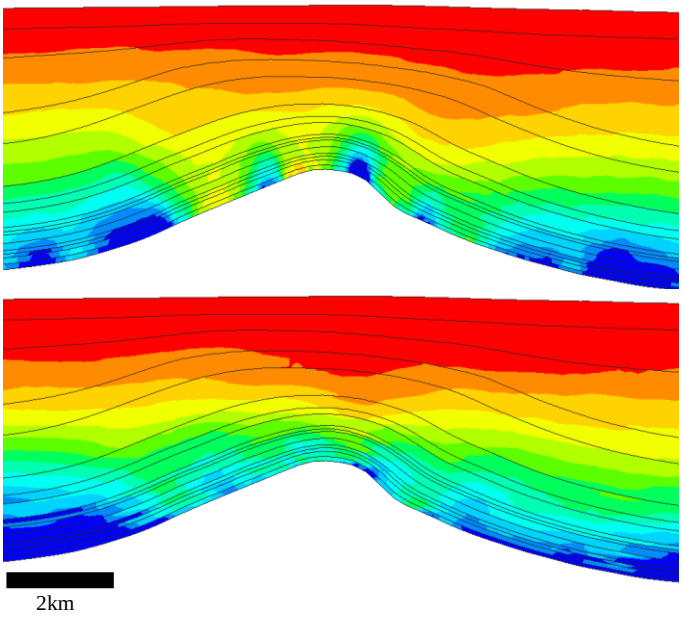

Fig.7. Vertical (upper) & horizontal (lower) effective stress distribution at present day for Case 2.

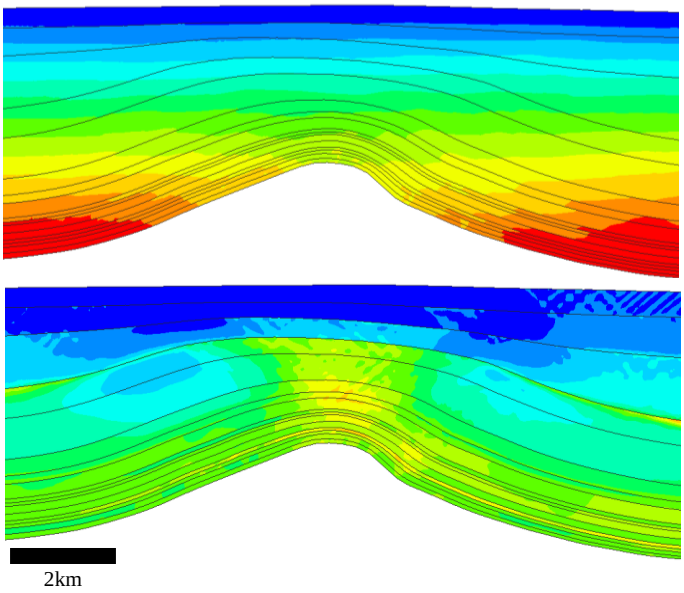

Fig. 8. Pore pressure (upper) & effective plastic strain (lower) distribution at present day for Case 2.

4.3. Case 3 - Nonlinear Basal Strains-Geomechanical Drained

ELFEN enables the specification of localized straining in the basal geometry as it motions from its initial to final position. Allowing the basal surface freedom to accommodate transverse lateral strains has a significant effect upon the predicted results. The most significant difference is the horizontal stress at the base of the model is far more compressive, in particular to the right of the crest (Fig. 9). This has led to a more dominant localization developing to the left of the anticline

(Fig. 10). Offset on this localization is more pronounced.

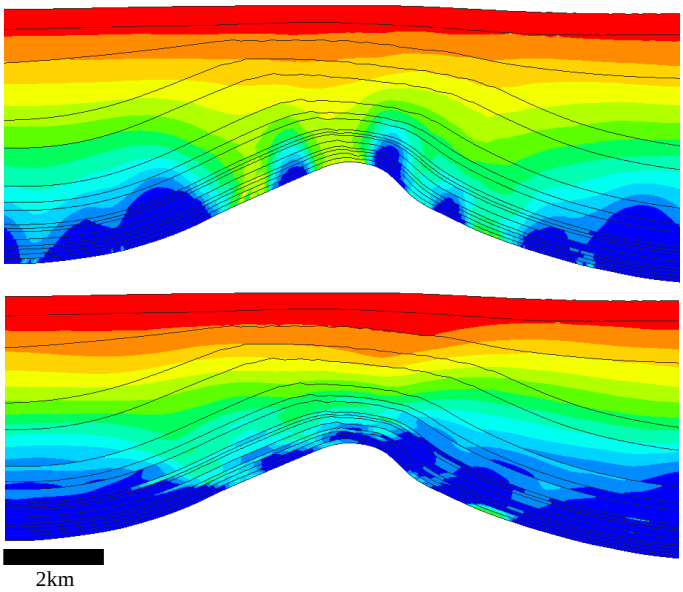

Fig. 9. Vertical (upper) & horizontal (lower) effective stress distribution at present day for Case 3.

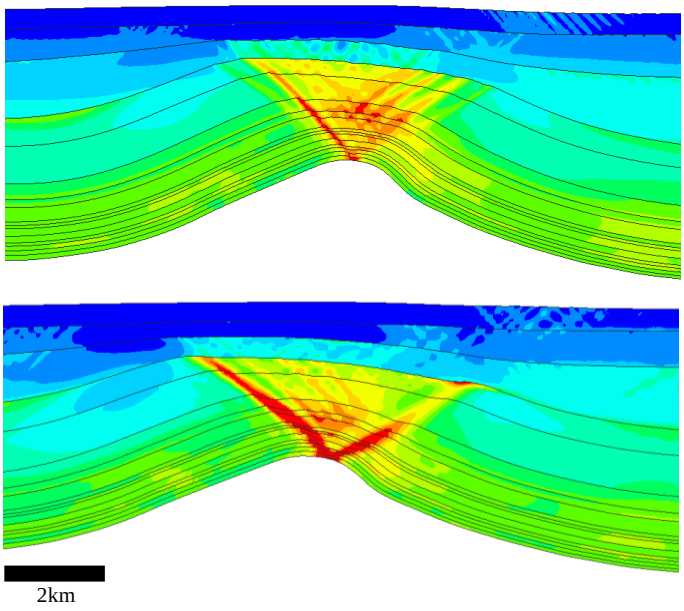

Fig. 10. Effective plastic strain distribution at present day for Cases 3 (upper) and 4 (lower).

4.4. Case 4 - Nonlinear Basal Strains-Geomechanical-Seepage Coupled

Introducing seepage flow has resulted in pore pressure being above hydrostatic over most of the region due to the tectonic shortening and the late rapid sedimentation, Fig. 11. It can be seen that the local non-linear straining at the crest has introduced local concentrations of high pore pressure distribution in the region of the crest. This case study shows a stronger localization than in case 2, where the base of the model is constrained (linear basal strains). Localizations are also more prominent than those observed in case 3 where drained, hydrostatic conditions appertain.

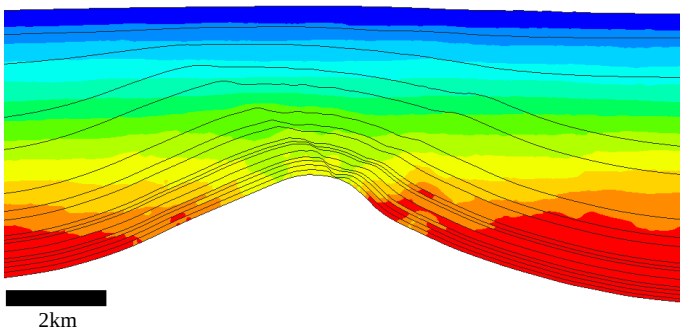

Fig. 11. Pore pressure at present day for Case 4.

4.5. Case 5 - Nonlinear Basal Strains with Additional Tectonic Shortening - Geomechanical Drained

Including further lateral shortening (1km) to the right hand boundary has introduced higher lateral stresses and an increase in the vertical stress on the right limb of the anticline, Fig. 12.

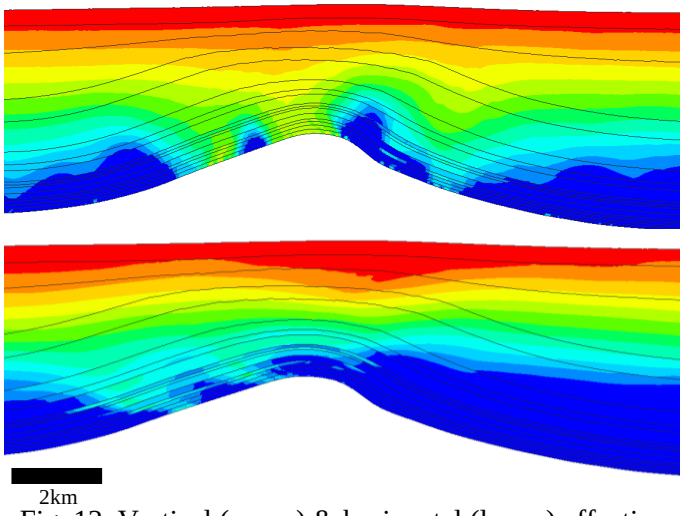

Fig. 12. Vertical (upper) & horizontal (lower) effective stress distribution at present day for Case 5.

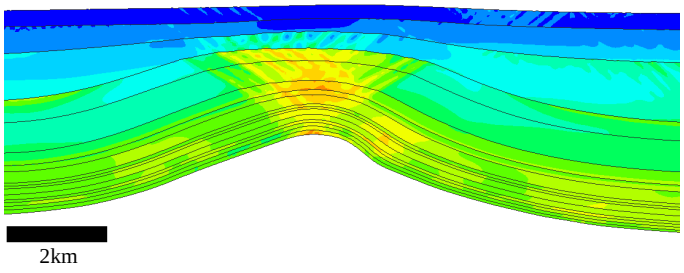

Fig. 13. Effective plastic strain distribution at present day for Case 5.

The consequence of the additional shortening is the suppression of the shear localizations above the crest, as highlighted by Fig. 13.

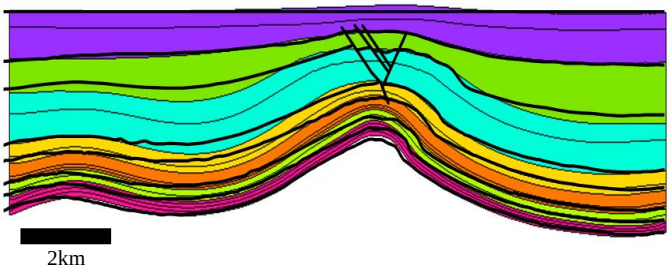

Fig. 14. Comparison of predicted present day horizon profiles for Case 5 and seismic horizons (thick lines).

The horizons interpreted from the seismic data are compared against the predicted current day profiles of case 5 in Fig. 14. Reasonable comparisons can be observed above the crest apart from the sharp localization interpreted from the seismic data to the right of the anticline.

4.6. Case 6 - Nonlinear Basal Strains with Additional Tectonic Shortening - Geomechanical-Seepage Coupled

The influence of the build-up of pore pressure resulting from the additional lateral shortening by accounting for the seepage flow can be clearly seen from the reduction in vertical and horizontal stresses compared with case 5 (which assumes drained conditions) and the formation of a strong shear localization above the crest which is absent in case 5. The pore pressures at 1km to the left of the crest are above hydrostatic from the sea bed all the way to the base of the Reservoir Series 2b layer. However, there is some pressure regression occurring below 2km. These pressures match reasonably well with field observations, Fig. 17.

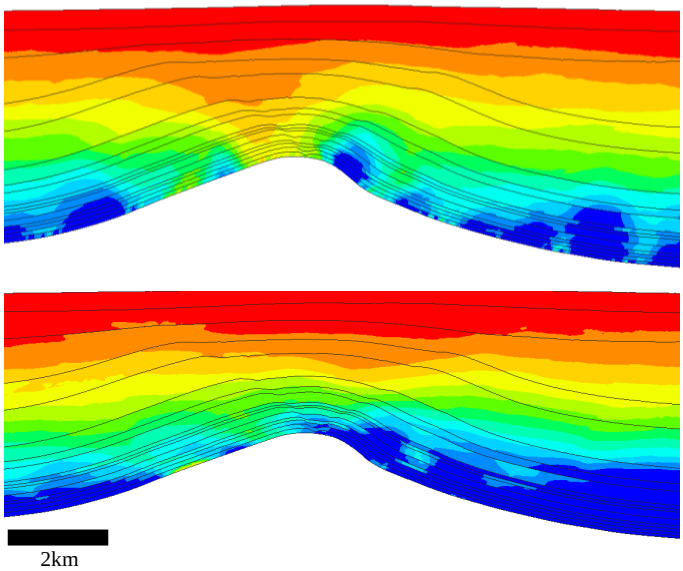

Fig. 15. Vertical (upper) & horizontal (lower) effective stress distribution at present day for Case 6.

5. CONCLUSION

The application of the forward modeling technology to the formation of the ACG anticline has highlighted several important aspects when considering the evolution of geological structures. One key aspect is the influence of overpressured systems. The case studies presented here have shown that localizations form more readily in regions that are overpressured. This increase in pore pressure, arising from either rapid sedimentation or lateral shortening, reduces the effective mean stress and increases the deviatoric stress, resulting in brittle shear failure as opposed to diffuse compaction.

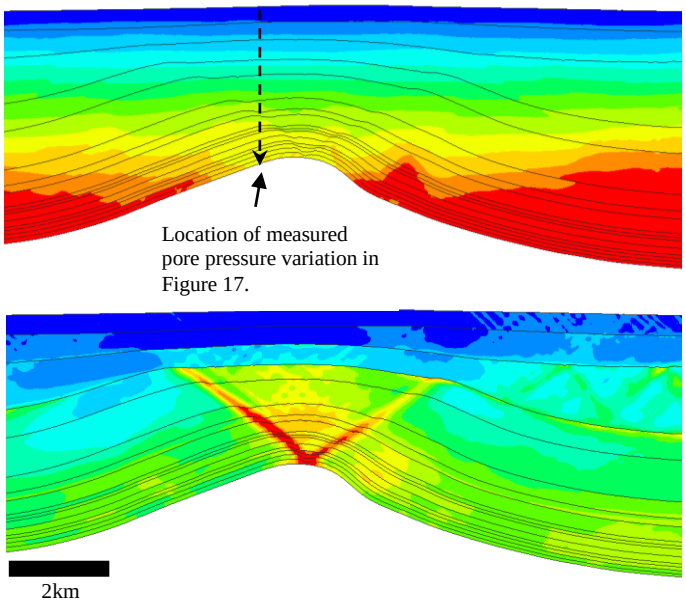

Fig. 16. Pore pressure (upper) and effective plastic strain (lower) distribution at present day for Case 6.

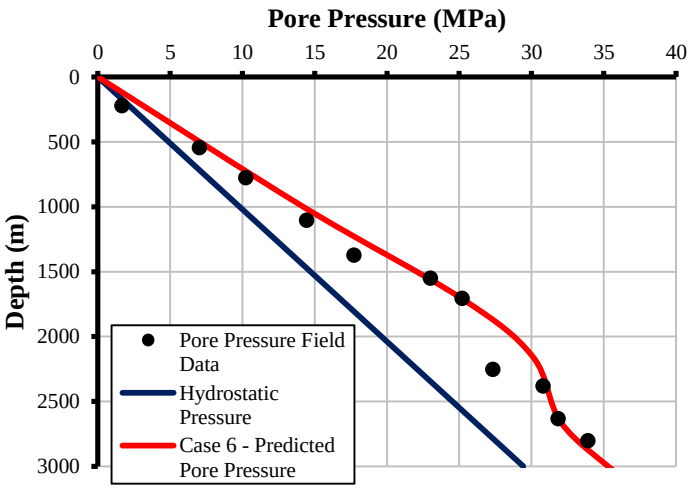

Fig. 17. Pore pressure variation with depth at a location 1km to the left of the crest.

Another aspect worth noting is that the stress state may undergo several different stress regimes in arriving at current day conditions, with the evolution of the material state being greatly dependent upon the stress path history. This is evident from the initial case, figure 3, where above the crest the stress state is initially lithostatic, followed by a period of highly reduced lateral stress only to be highly stressed in recent times due to lateral shortening. During the period of low horizontal stress the material above the crest was in a state of shear with several localizations forming. In more recent times the material is now compacted over and above that which would occur from just consolidation. Consideration of the transient evolution of the stresses and corresponding material state can give clues to the nature and integrity of sedimentary sequences that might have important roles in a petroleum system e.g. a reservoir, trap/seal.

Kinematic restorations usually assume a uniform linear variation of basal strain. The imposition of this condition can lead to the suppression of localized stress concentrations and hence the initiation of structures forming. This is highlighted by comparing case studies 1 and 3, where by allowing for non-linear basal strains in the region of the crest a graben forms. Also, by allowing the base of the model the freedom to accommodate transverse non-linear strains the variation in stress and pore pressure distribution may be greater.

The forward modeling technology has been used to successfully investigate the influence of several geological and material parameters providing reasonable comparisons with horizon profiles and in case 6 producing close approximations to the actual field pore pressure measurements.

However, the localization present to the right of the anticline crest has not been captured and it is thought that this is a result of not capturing correctly the evolution of the complex rheology and structures present in the basement units. Specifically, the stiffness and response of the reservoir and overburden units in the post-yield configuration may need refinement and a sensitivity analysis. Furthermore, the nature of the basement which is thought to behave in a more fluid, viscous manner (mud walls/mud volcanoes), is perhaps not adequately represented by the current evolving basal profiles. The seismic imaging is unfortunately not well defined in this region and therefore the FM technology will also be used to help constrain the influence of the basement.

ACKNOWLEDGEMENT

The authors wish to thank BP for permission to publish this paper and for funding aspects of this research. DR wishes to thank Rockfield Software Ltd, Cardiff University and the European Social Fund for funding his Ph.D. via a KESS scholarship.

REFERENCES

1. ELFEN Forward Modelling User Manual, 2010. Rockfield Software Limited.
2. Thornton, D. A., D.T. Roberts, A.J.L. Crook and J.G. Yu, 2011. Regional scale salt tectonics modelling: Bench-scale validation and extension to field-scale propblems. *Beyond balanced sections: Geological Society of America Conference, Minneapolis, USA*.
3. Albertz, M. and S. Lingrey. 2012. Critical state finite element models of contractional fault-related folding: Part 1. Structural Analysis. *Tectonophysics. Engrg*. 576. 133-149.
4. Peric, D. and A.J.L. Crook. 2004. Computational strategies for predictive geology with reference to salt tectonics. *Comput. Methods Appl. Mech. Engrg*. 193. 5195-5222.
5. Albertz, M. and P.F. Sanz. 2012. Critical state finite element models of contractional fault-related folding: Part 2. Mechanical Analysis. *Tectonophysics. Engrg*. 576. 150-170.
6. Crook, A.J.L., S.M. Wilson, J.G. Yu and D.R.J. Owen. 2006. Predictive modeling of structure evolution in sandbox experiments. *Journal of Structural Geology*. 28. 729-744.
7. Peric, D. and D.R.J. Owen, 1998. Finite element applications to nonlinear mechanics of solids. *Rep. Prog. Physics*. 61. 1495-1574.
8. Crook, A.J.L., S.M. Wilson, J.G. Yu and D.R.J. Owen. 2003. Computational modelling of the localized deformation associated with borehole breakout in quasi-brittle materials. *Journal of Petroleum Science and Engineering*. 38. 177-186.
9. Rudnicki, J.W. and J.R. Rice. 1975. Conditions for the localization of deformation in pressure-sensitive dilatant materials, *J. Mech. Phys. Solids*. 23, 371-394.
10. Belytschko, T., J. Fish and B.E. Engelman. 1988. A finite element with embedded localization

zones. *Comput. Methods. Appl. Mech. Engrg*. 176. 127-146.

11. Lewis, R.W., B.A. Schrefler, 1998. *The finite element method in the static and dynamic deformation and consolidation of porous media*. 2nd ed. Wiley.
12. Hantschel, T., A.I. Kauerauf, 2009. *Fundamentals of Basin and Petroleum Systems Modeling.* Springer.
13. Hossack, J. R., 1979, The use of balanced cross-sections in the calculation of orogenic contraction: A review, *Journal of the Geological Society of London*, 136, 705-711.
14. Jamison, W. R., 1987, Geometrical analysis of fold development in overthrust terranes, *Journal of Structural Geology*, 9, 2, 207-219.